Title

Phase stability and property evolution of biphasic Ti–Ni–Sn alloys for use in thermoelectric applications

Journal

Journal of Applied Physics, 115(4)

ISSN

0021-8979

Authors

Douglas, Jason E
Birkel, Christina S
Verma, Nisha
et al.

Publication Date

2014-01-28

DOI

10.1063/1.4862955

J. Applied Physics 115, 043720 (2014) DOI: 10.1063/1.4862955

Phase stability and property evolution of biphasic Ti–Ni–Sn alloys for use in thermoelectric applications

Jason E. Douglas,[1,2,a)] Christina S. Birkel,[2,3] Nisha Verma,[1] Victoria S. Miller,[1] Mao-Sheng Miao,[2] Galen D. Stucky,[3] Carlos Levi,[1] Tresa M. Pollock,[1,2] and Ram Seshadri[1,2,3]
[1)] *Materials Department, University of California, Santa Barbara, CA 93106*
[2)] *Materials Research Laboratory, University of California, Santa Barbara, CA 93106*
[3)] *Department of Chemistry and Biochemistry, University of California, Santa Barbara, CA 93106*

(Dated: 17 March 2013)

Thermoelectric properties and phase evolution have been studied in biphasic Ti–Ni–Sn materials containing full-Heusler $TiNi_2Sn$ embedded within half-Heusler thermoelectric TiNiSn. Materials prepared by levitation induction melting followed by annealing were of the nominal starting composition of $TiNi_{1+x}Sn$, with x between 0.00 and 0.25. Phases and microstructure were determined using synchrotron X-ray diffraction and optical and electron microscopy. The full-Heusler phase is observed to be semi-coherent with the half-Heusler majority phase. Differential thermal analysis was performed to determine melting temperatures of the ternary compounds and extrapolate a liquidus contour surface for the Ti–Ni–Sn system. The thermal conductivity is reduced in full-Heusler material. This leads to an increased thermoelectric figure of merit, ZT, from 0.35 for the stoichiometric compound to 0.44 for $TiNi_{1.15}Sn$. Density functional theory calculations using hybrid functionals (HSE06) were carried out to determine band alignments between the half- and full-Heusler compounds, as well as comparative energies of formation. The HSE06 band structure of TiNiSn is presented as well.

INTRODUCTION

Among the approaches suggested for increasing the energy efficiency of engineering systems, thermoelectric materials, which convert between thermal and electrical energy through solid-state phenomena, have received great interest. In particular, these materials have been suggested for devices that capture and utilize waste heat, such as in the exhaust from automobiles.[1,2] The proficiency of a material at thermoelectric energy conversion is captured in the dimensionless figure of merit, $ZT = (S^2\sigma/\kappa)T$, where S is the Seebeck coefficient, σ is the electrical conductivity, κ is the thermal conductivity, and T is the absolute temperature. In the past decade, a number of approaches have been employed to engineer improvements in ZT, including doping,[3] solid solutioning,[4] nanostructuring,[5] band structure engineering,[6] and crystal complexity,[7] leading to ZT values greater than 2 being reported in recent years.[8]

The physical properties that make up the figure of merit are interconnected, related to one another by the electronic structure, making it challenging to substantially increase the ZT of a material. For instance, S and σ are known to be negatively correlated.[3] However, by controlling the microstructure, it is possible to reduce the thermal conductivity without greatly impacting the electrical properties. In semiconductors, the thermal conductivity has two principle components: that arising from energy of charge carriers, κ_{el}, and that of lattice vibrations, κ_{lat}. While κ_{el} is tied directly to electrical conductivity by the Wiedemann-Franz Law, κ_{lat} can be controlled through alteration of the crystalline lattice and microstructure. For instance, embedding particles (both insulating[2] and semimetal[9]) within thermoelectric materials can disrupt phonon motion and reduce κ.

An opportune system for this type of microstructuring is a group of semiconducting compounds that form the half-Heusler crystal structure. These materials have been proposed as good thermoelectrics, most notably those based on TiNiSn. Half-Heusler XYZ compounds, where X and Y are typically transition metals and Z is a main group element, have a cubic unit cell of three interpenetrating face-centered cubic lattices, offset by a (1/4, 1/4, 1/4) translation. They are observed to have large values of S and σ, but suffer from high thermal conductivities, which can be four times that of telluride thermoelectrics.[3] A common technique to improve ZT in half-Heuslers is to reduce κ_{lat} by either subsitution of heavier, isovalent atoms at the X site[10,11] or the reduction of grain size[4]. It is also common to substitute an aliovalent element on the Z site to increase σ by electron or hole doping.[12]

Another avenue that has been pursued is to reduce the thermal conductivity of TiNiSn by inclusion of a secondary phase, notably the (full-)Heusler compound $TiNi_2Sn$.[13–15] We recently reported on the high-temperature properties of one such biphasic thermoelectric, $TiNi_{1.15}Sn$ as formed by a series of phase transformations.[16] A lower κ is observed in the biphasic materials, attributed to interfacial phonon scattering. This approach, using the Ti–Ni–Sn system, is attractive because the similarity of half- and full-Heusler crystal structures (∼3 % lattice mismatch), allowing for (semi-)coherent phase interfaces, leading to minimal disruption of the electronic properties.[15] Addi-

[a)] Electronic mail: jedouglas@mrl.ucsb.edu

tionally, $TiNi_{1+x}Sn$ is comprised of elements that are earth-abundant, non-toxic, and relatively inexpensive, which is not the case for many state-of-the-art thermoelectric materials; such attributes will be important if thermoelectrics are to gain widespread, industrial-scale usage.[2,17]

In exploring the introduction of additional phases to modify thermoelectric properties, it is important to have an understanding of system thermodynamics, so as to develop insight into how preparation techniques (and operation temperatures) will lead to different microstructures and phases in the material. Here, we present experimental and theoretical studies in the thermodynamics of the Ti–Ni–Sn ternary system, using differential thermal analysis to construct a liquidus surface, as well as first-principles calculations to compare free energies of the intermetallic compounds—a calculated isothermal section of the ternary phase diagram at 0 K is included. These experiments help to explain the common presence of impurity phases in stoichiometric TiNiSn, as reported by other researchers.[10]

We also report on the observed microstructural development, thermoelectric properties, and band alignment of biphasic materials of the starting composition $TiNi_{1+x}Sn$, with x between 0.00 and 0.25, as prepared by magnetic levitation induction melting. While this technique has been utilized previously in thermoelectric preparations, typically the resulting ingots were subsequently ball-milled, which is not done in this study.[18] Additionally, the secondary phase has not been physically implanted but, rather, evolves based on starting composition of the melt. The resultant microstructure and effects of heat treatment are discussed, as well as insights from density functional theory on the electronic structures of TiNiSn and $TiNi_2Sn$, using both the generalized gradient approximation and hybrid functionals.

METHODS

Experimental Details

Preparation

For the study of thermoelectric properties, six samples were prepared with the nominal starting composition $TiNi_{1+x}Sn$ with $x = 0.00$, 0.05, 0.10, 0.15, 0.20, and 0.25. Compositions were chosen to be within the biphasic region between TiNiSn and $TiNi_2Sn$ based on the reported phase diagrams.[19,20] This permits the effect of $TiNi_2Sn$ phase fraction within the TiNiSn bulk to be investigated. Two additional compounds, stoichiometric TiNiSn and $TiNi_2Sn$, were made for thermal analysis. The starting materials were Ti rod (99.7%, Sigma-Aldrich), Ni foil (≥99.9%, Sigma-Aldrich), and Sn shot (99.8%, Sigma Aldrich).

The materials were prepared from ∼ 20 g charges under an Ar atmosphere using a Crystalox MCGS5 induction levitation melting system with a water-cooled copper crucible. Charges were held molten for 120 s and then rapidly cooled. The resultant buttons were then wrapped in tantalum foil, sealed in evacuated fused-silica ampoules, and annealed for 24 h at 1173 K, followed by 192 h at 1123 K. All samples had 93% relative density or greater.

Characterization

All specimens for characterization were sectioned directly from the annealed ingots. Powder X-ray diffraction (XRD) patterns were acquired with a Philips X'Pert Powder Diffractometer with CuKα radiation on crushed and ground material. Scans were 30 minutes, from $2\theta = 10°$ to 120°. Additionally, room temperature, powder synchrotron radiation XRD data was collected at the Advanced Photon Source (APS) at Argonne National Laboratory, using the 11-BM beamline. The patterns were analyzed using the Rietveld method as implemented in the XND code,[21] from which phase fractions were determined.

Sections from the center of the bulk were examined using various metallographic techniques. All samples were epoxy-mounted and polished, with 0.25-micron diamond suspension used for the final polish. Samples for electron backscatter-diffraction analysis (EBSD) were subsequently polished for 4 h with colloidal silica. Scanning electron microscopy (SEM) was performed using an FEI XL30 Sirion FEG Microscope equipped with a backscattered-electron (BSE) detector, which allowed for greater distinction between phases. Electron backscatter diffraction analysis (EBSD), with energy-dispersive X-ray spectroscopy (EDX) assistance, was carried out using an FEI Dualbeam focused ion beam (FIB) microscope.[22] Light-optical micrographs were captured with QImaging software. Transmission Electron Microscopy (TEM) was performed on the FEI Tecnai G2 Sphera microscope, on lamellae fabricated by FIB milling.

Differential thermal analysis (DTA) was performed on a Setaram SETSYS Evolution TGA for two specimens of TiNiSn and $TiNi_2Sn$ each, with a temperature ramp rate of 5 K per minute. The half-Heusler compounds were measured from 1073 K to 1548 K and 1073 K to 1673 K, while the Heusler compounds were measured from 1073 K to 1673 K and 1073 K to 1848 K. X-ray diffraction patterns were taken before and after each measurement. Thermal diffusivity of $TiNi_{1+x}Sn$ compounds was measured between room temperature and 873 K under Ar by an Anter Flashline 5000, which utilizes the thermal flash technique. Specimens, which were approximately 7.5 mm in diameter and 1.25 mm thick, were sprayed with carbon paint to minimize errors in emissivity. Data was analyzed using the Cowan model and Dulong-Petit heat capacity, $C_p = 3R/M$, where R is the gas constant and M is the atomic molar mass. Seebeck coefficient and electrical resistivity were measured in three cycles between

room temperature and 873 K on the Ulvac-Riko ZEM-3, with He atmosphere underpressure (−0.08 MPa). Measured specimens were rectangular bars, approximately 2 mm×2 mm×10 mm.

Computational Details

The electronic structure and formation energies of compounds in the Ti–Ni–Sn ternary were investigated using the Vienna *ab-initio* Simulation Package (VASP).[23,24] Pseudopotentials utilized the projector-augmented wave (PAW) method.[25] To explore the band alignment between $TiNi_2Sn$ and semiconducting TiNiSn, a slab model was employed, with the Perdew-Burke-Ernzerhof generalized gradient approximation functional (GGA-PBE) for the exchange-correlation energies and potentials.[26] Using supercells of approximately 6 Å×4 Å×70 Å,—equivalent to *ca.* 8 TiNiSn unit cells stacked along the z-direction—with half of the cell being vacuum and the non-polar (110) plane as the crystal surface, the difference between vacuum and the Fermi energy of the crystal was determined. Band structures were calculated using a combination of local density approximation using the Hubbard U correction parameter (LDA+U)[27] and hybrid functionals, incorporating exact exchange from Hartree-Fock theory, specifically the Heyd-Scuseria-Ernzerhof (HSE06) exchange-correlation functional.[28]

To explore the enthalpies of formation, GGA-PBE with a gamma-centered **k**-mesh of 8×8×8 was utilized for all compounds, with an energy cutoff of 550 eV. Both Methfessel-Paxton and tetrahedron smearing methods were used, with full electronic and atomic structural optimization. All calculations were spin-polarized, with each Ni atom prescribed to have an initial moment of 3 μ_B.

PHASE AND MICROSTRUCTURE

Structure and Microscopy

Powder synchrotron X-ray diffraction patterns of the six $TiNi_{1+x}Sn$ samples analyzed for thermoelectric properties are shown in Figure 1. As the ratio of Ni to TiSn increases, so does the observed full-Heusler phase fraction, most clearly discernible by the growth of the Heusler peak at $Q = 2.92$ Å^{-1}. In all but the TiNiSn compound, all observable peaks in XRD data collected by X'Pert could be indexed to the Heusler and half-Heusler phases. While impurity peaks did appear in synchrotron data of every sample, the refined phases fractions combined to ≤ 1 mol-%. No trend is seen in refined lattice parameter, a, for the Heusler phase: a mean value of 6.081 Å with a spread of 1 pm. The half-Heusler lattice parameter increased steadily in accordance with Vegard's law until $TiNi_{1.10}Sn$, with subsequent Ni additions having little effect on the lattice parameter, a. (Fig. 2 (a).) This suggests that there may be a degree of Ni solutioning into the half-Heusler, in spite of thefact that equilibrium TiNiSn is reported to be a line compound.[20]

In the $x = 0.00$ material, which could be expected to be single phase, three additional phases are formed: $TiNi_2Sn$, Ti_6Sn_5, and Sn, together constituting approximately 5 mol-% of the bulk. A diffractogram highlighting

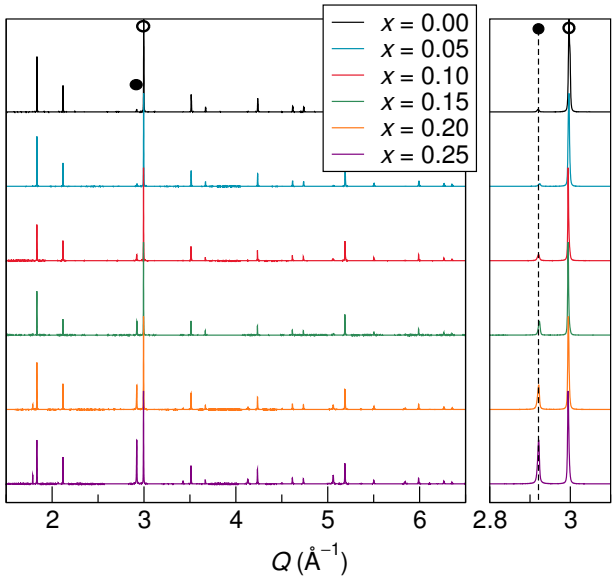

FIG. 1. Powder synchrotron X-ray diffractograms of $TiNi_{1+x}Sn$ samples. With increasing Ni content, Heusler-phase peak intensities increase with respect to those of the half-Heusler. Magnified view of the main peaks (filled circle: Heusler, empty circle: half-Heusler) are shown to the right.

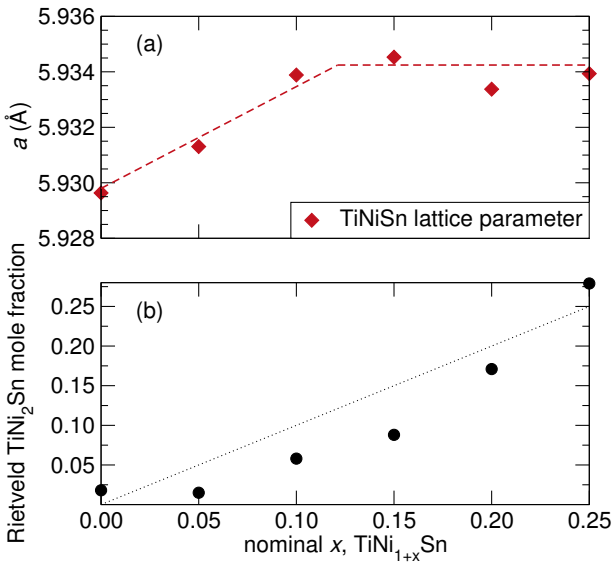

FIG. 2. (a) Lattice parameter of TiNiSn and (b) Heusler phase fraction as determined from scale factors of Rietveld refinement, as a function of x in $TiNi_{1+x}Sn$. Dashed line in (a) is a guide to the eye. Dotted line in (b) represents a 1:1 nominal to refined Heusler fraction. One-σ error bars are smaller than the width of points.

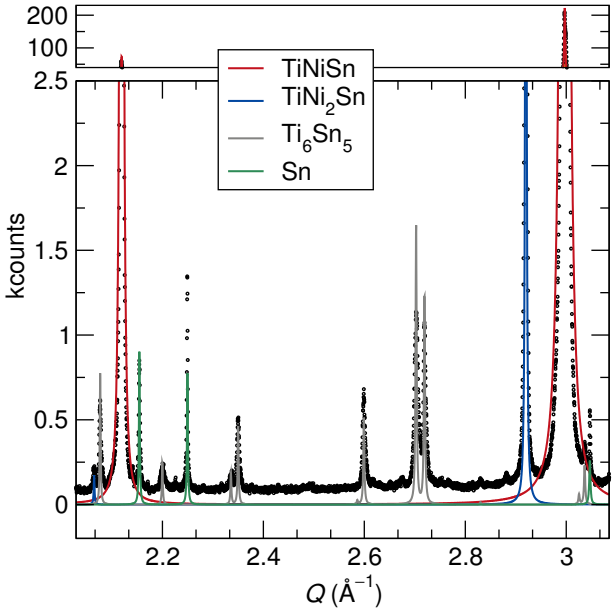

FIG. 3. Rietveld refinement of powder synchrotron X-ray diffraction pattern for $x = 0.00$ TiNiSn, magnified to show impurity peaks, including $TiNi_2Sn$, Ti_6Sn_5, and Sn. Though the intensities of these impurity peaks were much greater in the stoichiometric half-Heusler material, small peaks associated with Ti–Sn binary and Sn phases were discernable in all synchrotron patterns.

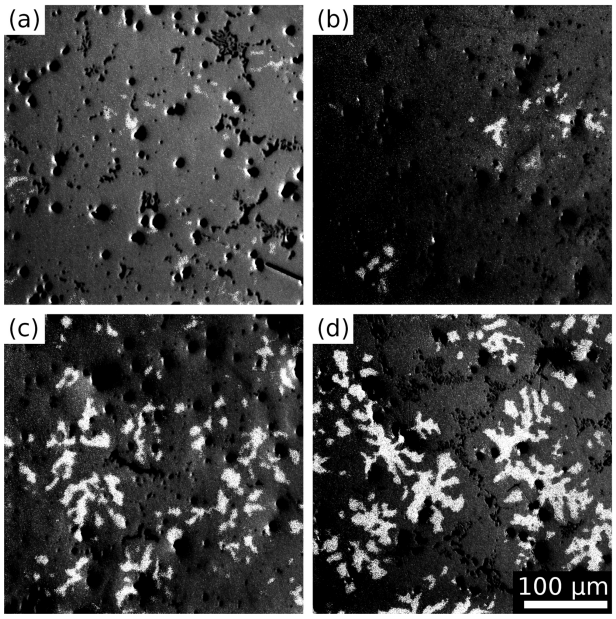

FIG. 4. Light-optical microscope images of polished specimens (a) $x = 0.00$, (b) $x = 0.05$, (c) $x = 0.15$, and (d) $x = 0.20$. Light regions are Heusler phase, charcoal are half-Heusler. Black circles are pores. Some Ti_6Sn_5 impurity is also observable in (a), dark gray impressions.

the impurity peaks with the greatest counts is presented in Figure 3. These impurities persisted through multiple attempts of melting and annealing of stoichiometric TiNiSn, and are believed to be principally a consequence of segregation in the liquid as samples were cooled, as prescribed by the liquidus surface. This topic is discussed in detail in the following section.

To investigate the distribution, morphology, and interfaces of these $TiNi_2Sn$ precipitates, metallographic techniques were employed. It was found that the Heusler and half-Heusler phases could be distinguished by light optical microscopy by lowering the gamma correction in the image capturing software. Such micrographs of four alloys are presented in Figure 4. The half-Heusler phase appears continuous and contains embedded islands of the full-Heusler phase. The full-Heusler phase regions are on the order of 10-20 μm, similar to the average bulk grain size, and generally dendritic in morphology. The shape of these particles is indicative of solidification in a liquid medium, suggesting that they freeze first.[29] As the nickel content was raised, so too was the area-fraction of $TiNi_2Sn$ particles, which agreed well with the Rietveld analysis. The precipitates were largely isolated in the samples $0.00 \leq x \leq 0.15$, but become more continous, large dendritic channels in $Ni_{1.20}TiSn$, in excess of 200 μm.

Viewing the full-Heusler phase regions at higher magnification, Fig. 5, embedded TiNiSn particles are apparent, producing a sponge-like morphology. Though only the largest TiNiSn precipitates could be resolved by optical microscopy, backscatter electron (BSE) dection SEM confirmed that most Heusler particles have a fine "cellular" structure. BSE was necessary, as the Heusler phase was not discernible using secondary electron detection. In multiple specimens small amounts of $Ti_5Ni_xSn_3$ are observed, though not detected by X-ray diffraction. Within the Heusler region, a number of nanometer scale TiNiSn inclusions, both circular and needle-shaped, are interposed between larger $\sim$1 μm half-Heusler precipitates. Micron-scale $TiNi_2Sn$ islands are observed in the half-Heusler bulk near a number of phase interfaces.

These precipitates within the Heusler phase are a result of the thermal cycle imposed on the materials. As recently reported by Romaka *et al.*, the $TiNi_2Sn$ phase region extends further towards TiNiSn at high temperatures, reducing the size of the two-phase field.[20] Following the lever rule, when the material that had been heated at 1173 K slow cools, decreasing solubility in the Heusler phase causes TiNiSn particles to precipitate out. This fine intermixing between phases occurs during the annealing period, 192 h at 1123 K, when substantial Oswald ripening could also have been expected to occur. Both scales of phase segregation ($\sim$20 μm, $\leq$1 μm) are expected to influence the measured transport properties. Biswas *et al.* recently discussed how microstructuring over a wide spectrum of lengths could be beneficial to reaching optimal thermoelectric properties.[8]

To gain understanding of the microstructure and to confirm the composition of the regions observed in optical and SE microscopy, the $TiNi_{1.15}Sn$ material was an-

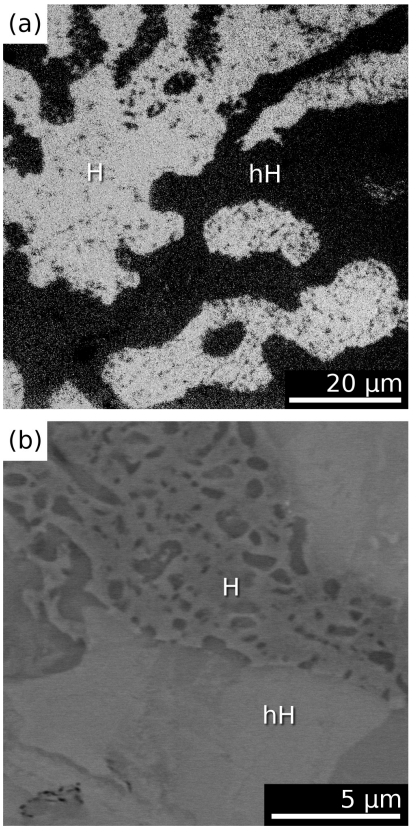

FIG. 5. Structure at the microscale showing distribution of full-Heusler precipitates, as seen in micrographs of the polished specimens. (a) Optical microscopy of $x = 0.20$ material. Lighter areas are Heusler (H) phase, charcoal regions are half-Heusler (hH) bulk. (b) Backscatter mode SEM, $x = 0.15$. hH precipitates (dark) within the $TiNi_2Sn$, on the order of 100 nm.

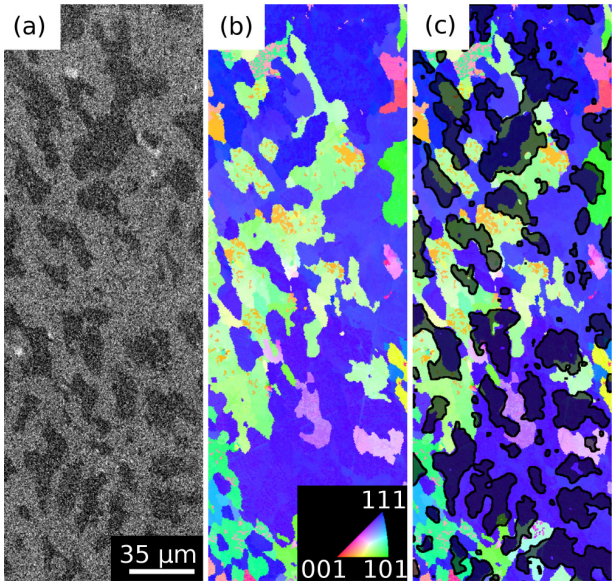

FIG. 6. (a) EDX map of Sn distribution, dark areas being poor in Sn and (b) inverse pole figure map of the same $100 \times 200\,\mu$m region of the $x = 0.15$ specimen. The two maps are overlayed in (c). The Sn poor regions are $TiNi_2Sn$, while the Sn rich is TiNiSn. Both full- and half-Heusler particles are observed within regions of the same crystallographic orientation, suggesting interfacial coherence. (Color online.)

alyzed using EBSD. Due to the similarity of the Heusler and half-Heusler crystal structures, and therefore their diffraction patterns, EDX data was collected to distinguish TiNiSn from $TiNi_2Sn$, run concurrently with EBSD to determine low angle and high angle misorientation interfaces.

Displayed in Figure 6(a) is an EDX map for Sn distribution in the material, as Sn gives the highest counts and therefore highest contrast between phases, and Fig. 6(b) is the inverse pole figure map of the same data. The material contains a large region of connected material with a near-[111] orientation, over 300 μm in length. As can be seen in Fig. 6(c), the overlay of 6(a) and 6(b), while phase boundaries sometimes correspond to changes in orientation, they often do not. For example, the large [111] region in the bottom third of the mapped area contains almost equal amounts of half- and full-Heusler. This crystallographic alignment strongly supports the semi-coherency of $TiNi_2Sn$ with TiNiSn due to similarity of crystal structure. As shown by DTA data presented in the next section, the full-Heusler phase freezes first, it is believed that the half-Heusler matrix will adopt the orientation of nearby $TiNi_2Sn$ particles during the solidification process, leading to these large regions of similar orientation.

To characterize these TiNiSn/$TiNi_2Sn$ interfaces, TEM analysis was performed on lamellae taken from the $TiNi_{1.15}Sn$ material, prepared by focused ion beam (FIB) milling. It was verified with EDX that the particles within Heusler phase are half-Heusler TiNiSn and that the particles are semi-coherent; electron diffraction patterns across phase interfaces showed that phases are of the same crystallographic orientation. A representative micrograph is presented in Figure 7, showing a smaller (1 μm) $TiNi_2Sn$ particle within the TiNiSn matrix. Characteristic lattice misfit dislocations are present along the phase boundary. Further TEM on this system will be presented in future correspondence.

Differential Thermal Analysis and the Liquidus Surface

Differential thermal analysis was performed on the two end-member compounds, with the goal of gaining information to develop heat treatments. Though the decomposition of TiNiSn has been reported previously, the authors are unaware of any data on the thermal properties of $TiNi_2Sn$.[30] The heating curves are shown in Figure 8; all events were mirrored during cooling. In each of four distinct measurements, a specimen was heated to and cooled from a temperature indicated by circles in Fig. 8. The samples were then analyzed post-measurement by

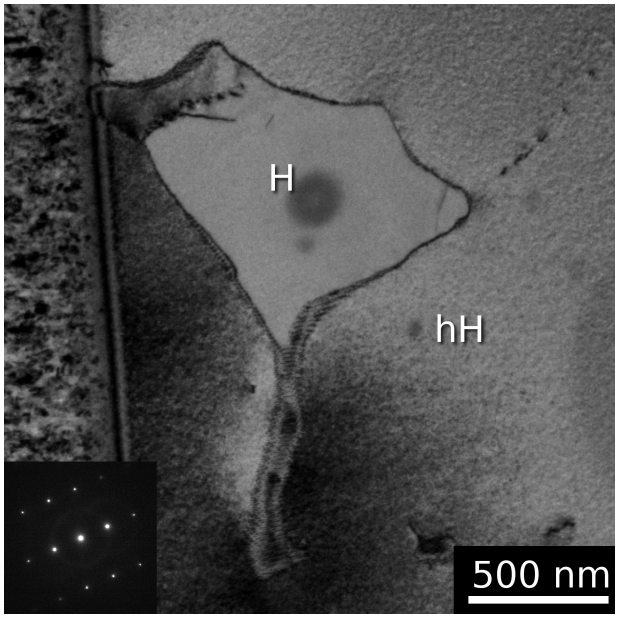

FIG. 7. TEM micrograph of Heusler particle, 1 μm in half-Heusler matrix, taken in bright field condition. Misfit dislocations can be observed along lower tip of $TiNi_2Sn$ phase. Included is the selected area diffraction pattern of particle and matrix.

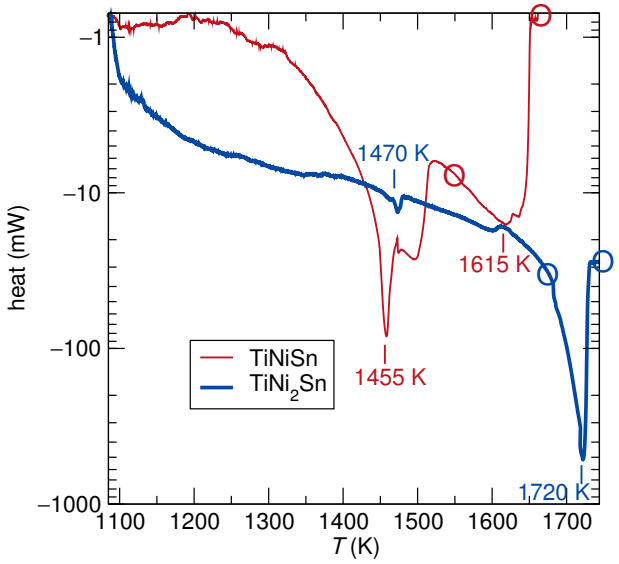

FIG. 8. Differential thermal analysis curves of TiNiSn (red) and $TiNi_2Sn$ (blue) during heating . TiNiSn showed three endothermic events, first melting at 1455 K. $TiNi_2Sn$ has a single melting event, at 1720 K. Each compound was analyzed in two separate measurements, to temperatures marked by circles. Powder X-ray diffraction was recorded on experimental products.

powder XRD (not shown).

The TiNiSn compound melts incongruently. The first melting event, as reported by Jung *et al.*, happens at 1455 K, in which TiNiSn decomposes into Sn, Ti_6Sn_5, and $TiNi_2Sn$. At 1615 K, a second reaction occurs, with Ni_3Sn_4 replacing Sn in the products, determined by powder XRD post-measurement. For $TiNi_2Sn$, no melting occured until 1720 K, again suggesting that the Heusler particles freeze first. The small peak at 1470 K is thought to be the result of a minor third phase, though none was discernible in the XRD pattern of the annealed source material.

Using these measurements, along with data from published binary phase diagrams,[31–33] a liquidus surface for the Ti–Ni–Sn ternary was constructed (Fig. 9). The half-Heusler composition, in the center of the ternary, sits in a liquidus chute. Though not a eutectic point, due to the exceedingly low melting point of Sn, the TiNiSn liquidus is lower than that of any other reported compound in the ternary—the Ti–Sn compounds in particular are 400-500 K higher. This lends insight into why phase-pure TiNiSn is difficult tp make from the melt, an issue that has been noted previously for this system.[10] As the charge cools, the high freezing point Ti_6Sn_5 (1763 K) solidifies first, as evidenced by the dendritic microstructure of the phase. (Note this compound shares a two-phase field with TiNiSn as well.) This event pushes the composition of the melt towards Ni, causing the formation of $TiNi_2Sn$ and a Ni–Sn binary. In $TiNi_{1+x}Sn$ compounds, as x increases the composition moves away from metastable Ti–Sn compounds that are likely to freeze

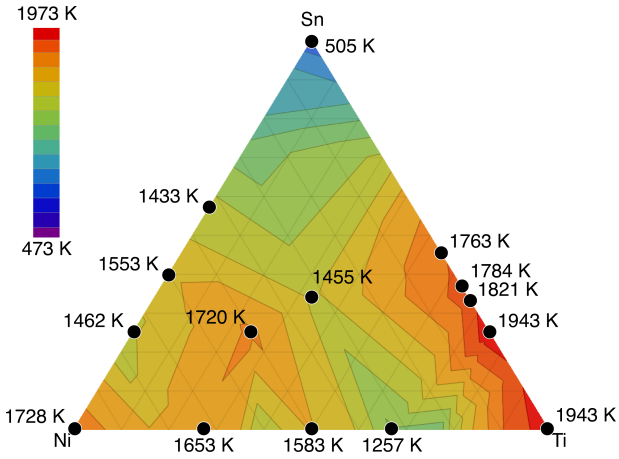

FIG. 9. Extrapolated countour map of the liquidus temperatures of Ti–Ni–Sn ternary (analogous to a liquidus surface). Local temperature maxima exist in Ti-rich Ti–Sn binaries, Ni, and $TiNi_2Sn$. The "valley"-like location of TiNiSn makes phase-pure synthesis difficult from the melt. Reported liquidus temperatures of known compounds are included.

preferentially over the desired phases and up in liquidus temperature, possibly explaining the absence of significant impurities in the $x > 0.00$ materials. Thus, to achieve truly phase-pure TiNiSn, the initial preparation method must be chosen carefully.

TABLE I. Enthalpies of formation at 0 K of various Ti–Ni–Sn compounds. For ternary compounds, the "stability," or the energy difference between their ΔH_f and the convex hull formed by the binary enthalpies, is included as well.

Compound	Space Group	ΔH_f (kJ mol^{-1})	Offset (kJ mol^{-1})
Ti	$P6_3/mmc$		
Ni	$Fm\bar{3}m$		
Sn	$I4_1/amd$		
Ti_6Sn_5	$P6_3/mmc$	−36.7	
Ti_5Sn_3	$P6_3/mmc$	−33.6	
Ti_2Sn	$P6_3/mmc$	−32.7	
Ti_3Sn	$P6_3/mmc$	−29.0	
Ti_2Ni	$Fd\bar{3}m$	−27.8	
TiNi	$Pm\bar{3}m$	−39.6	
$TiNi_3$	$P6_3/mmc$	−46.1	
Ni_3Sn	$P6_3/mmc$	−23.9	
Ni_3Sn_2	$Pnma$	−31.2	
Ni_3Sn_4	$C2/m$	−26.9	
TiNiSn	$F\bar{4}3m$	−69.0	−34.7
$TiNi_2Sn$	$Fm\bar{3}m$	−60.0	−25.9
Ti_2Ni_2Sn	$P4_2/mnm$	−46.8	−10.7
Ti_5NiSn_3	$P6_3/mcm$	−37.4	−1.5

Formation Enthalpies and 0 K Isothermal Section of Ti–Ni–Sn Ternary

To assess the stability of the two compounds and thermodynamics of Ni addition in $TiNi_{1+x}Sn$, the enthalpies of formation, ΔH_f, of TiNiSn and $TiNi_2Sn$ were calculated, and then compared to the energy hull of the Ti–Ni–Sn ternary, using the enthalpies of the various binary compounds. Enthalpy of formation was defined by

$$\Delta H_f(Ti_xNi_ySn_z) = E^{min}_{Ti_xNi_ySn_z} - \frac{xE^{min}_{Ti} + yE^{min}_{Ni} + zE^{min}_{Sn}}{x+y+z}, \quad (1)$$

where E^{min}_i is the minimum total energy per atom of the compound as calculated by DFT. Enthalpy of formation was determined for the ten reported binary compounds of the system, and used to construct an energy hull. The trends in ΔH_f along the binaries compared favorably to studies in the literature of structural stability in the Ni–Ti, Ti–Sn, and Sn–Ni systems.[46–48] Once this hull was formed, the difference between it and the ΔH_f of each ternary compound was determined. The results are presented in Table I. ΔH_f was −69.0 kJ/mol for TiNiSn, −60.0 kJ/mol for $TiNi_2Sn$. From this calculation, it was determined that the enthalpy of formation of TiNiSn is 0.360 eV below the hull as opposed to 0.268 for the full-Heusler, implying it is the more energetically favorable of the two compounds. Ti_2Ni_2Sn and Ti_5NiSn_3, which sit closer to the energy hull, are not observed experimentally to be stable except at high temperatures.[20]

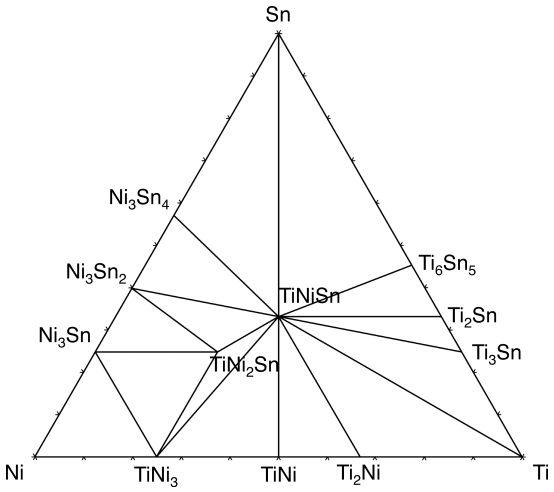

FIG. 10. Calculated isothermal sections of the Ti–Ni–Sn ternary phase diagram at 0 K, as found by relaxing reported compound structures. Among the four experimentally reported ternary compounds, only the half- and full-Heusler are stable at this temperature. The Ti_5Sn_3 is also above the ground state, thus not present.

This temperature dependence of compound formation is further elucidated by the "ground state" 0 K isothermal section of the ternary phase diagram, as calculated using Equation (2):

$$G_c^{Ti_{\dot{x}}Ni_{\dot{y}}Sn_{\dot{z}}}(T) = \dot{x}^0G^{\mathrm{HCP}}_{\mathrm{Ti}} + \dot{y}^0G^{\mathrm{FCC}}_{\mathrm{Ni}} + \dot{z}^0G^{\mathrm{Sn}}_{\mathrm{Sn}} + A^{Ti_{\dot{x}}Ni_{\dot{y}}Sn_{\dot{z}}} + B^{Ti_{\dot{x}}Ni_{\dot{y}}Sn_{\dot{z}}}T \quad (2)$$

Here $\dot{x}$, $\dot{y}$, $\dot{z}$ are the normalized chemical formulae values, ${}^0G^i_j$ is the molar Gibbs free energy of the elemental compound, i, in its ground state structure, j, as taken from the SGTE database.[49] A and B are the compound enthalpy and entropy of formation, respectively. At 0 K, the B parameter can be ignored. Of the reported intermetallic compounds, Ti_2Ni_2Sn, Ti_5NiSn_3, and Ti_5Sn_3 are found to lie above the ground state planes of the Ti–Ni–Sn system, and are therefore not stable at low temperatures, which again corresponds well with reported experimental diagrams,[19,20] This implies that these compounds are stabilized by entropic contributions, and therefore, their presence in Ti–Ni–Sn thermoelectrics may be influenced the temperature of preparation and device operation.

PHYSICAL PROPERTIES

Electronic Transport Properties

The temperature dependence of the electrical conductivity, σ, Seebeck coefficient, S, and power factor, $S^2\sigma$

TABLE II. Heusler phase fraction as determined by Rietveld refinement as well as area fraction of optical micrographs. Both show an increasing $TiNi_2Sn$ fraction with increasing Ni, though area fraction values tend to be greater than the Rietveld calculation.

x, $TiNi_{1+x}Sn$	H mol-%, XRD	ρ, 300 K (g cm^{-3})	σ, 300 K (S cm^{-1})	S, 300 K (μV K^{-1})	κ, 300 K (W m^{-1}K^{-1})	ZT, 800 K
0.00	2	7.19	99	-242	7.7	0.34
0.05	2	7.04	83	-242	7.1	0.38
0.10	6	6.96	173	-218	6.8	0.40
0.15	9	6.79	129	-223	5.5	0.43
0.20	17	7.26	404	-101	6.9	0.23
0.25	28	7.3	450	-125	6.4	0.31

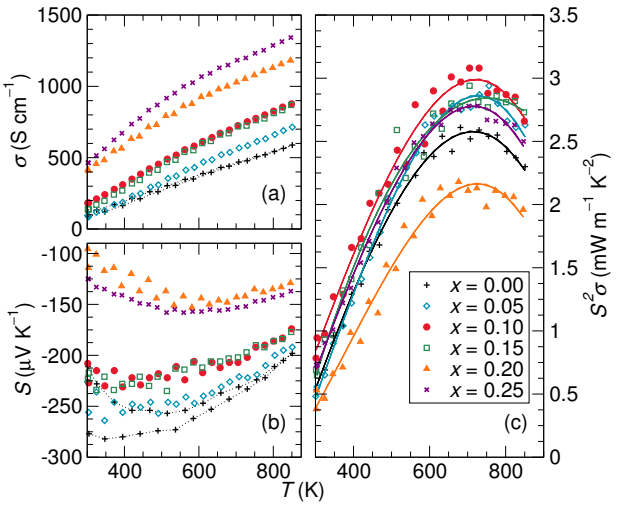

FIG. 11. Electronic transport data of $TiNi_{1+x}Sn$ samples. (a) Electrical conductivity increases monotonically with increasing Ni content, while the magnitude of the (b) Seebeck coefficient decreases. These offset one another for generally consistent (c) power factor values, $S^2\sigma$, save for $TiNi_{1.20}Sn$. Fitted lines are shown as guides to the eye.

are displayed in Figure 11. Although each sample was measured over three heating cycles, only the first is displayed for clarity. In a previous study we have witnessed large changes in properties upon heating,[34] but the measured values for the present materials remained consistent through every cycle. Only the $x = 0.00$ sample showed significant change, a 18% drop in its Seebeck value at 300 K. However no further degradation of properties was seen. The data of successive cycles is in line with the first cooling values. Previous measurements suggested this drop to be caused by evolution of minor phases during heating, which is consistent with the fact that it is most pronounced in our impure TiNiSn compound.[34]. The data for TiNiSn is comparable to those reported in literature.[10,12]

The measured electrical conductivity, in Figure 11(a), was highly responsive to the change in x. All samples are semiconducting in character, with σ increasing with tempearture, even at the highest Heusler phase fraction. Higher Ni content corresponds unambiguously to larger σ.

The magnitude of the Seebeck coefficient decreases with increasing x, as is expected given the trend in electrical conductivity, which is known to correlate negatively with $|S|$.[3] The response of S to T reaches a minimum then begins to increase as more carriers are excited, though there is variance among the materials as to the temperature at which this occurs. For instance, the minimum occurs at a significantly higher temperature for $TiNi_{1.20}Sn$ and $TiNi_{1.25}Sn$ than for the other samples, closer to room temperature. The value of S is strongly related to the nature of the band gap of a material,[35] so the change in temperature dependence may correspond to a change in the band filling due to varying occupancy of Ni in the empty tetrahedral site of the half-Heusler structure. Hazama *et al.*[14] note that these "interstitials" can cause in-gap states, reducing the effective band gap. Our refined XRD data found that the prevalence of these interstitials was about half as great in the $x = 0.20$ and 0.25 materials, which may explain the higher turnover temperature.

In both Seebeck coefficient and electrical conductivity, there is a large gap between the measured values of the two highest-Ni materials and the other samples, suggesting that there is some difference in transport mechanisms, likely arising from differences in microstructres. As can be seen in Figure 11(c), the changes in S and σ almost perfectly offset each other, with four of six power factor curves lying overlapping at high temperatures, approaching a peak value of 3×10^{-3} W·m^{-1}K^{-1}. The only significant outlier is the $x = 0.20$ compound. Though the $x = 0.25$ sample has a similarly low Seebeck coefficient, both it and the electrical conductivity are greater leading to a power factor similar to the best samples. Between these two samples, the typical S-σ relation is inverted, likely due to differences in microstructure; though large connectivity was observed in both materials, it is more pronounced in $TiNi_{1.20}Sn$.

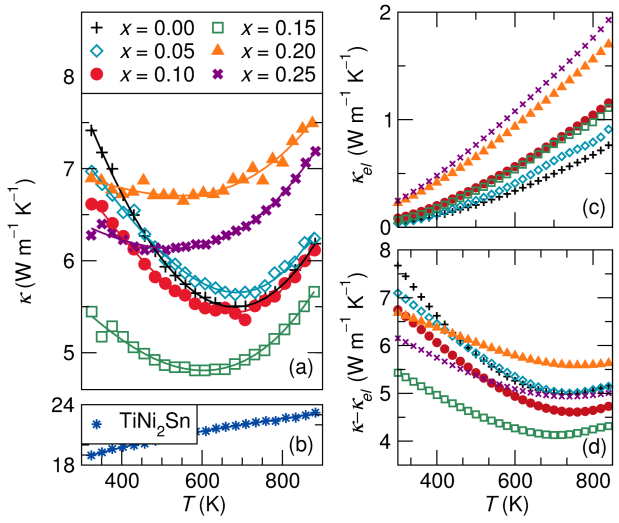

FIG. 12. Measured thermal conductivity of (a) $TiNi_{1+x}Sn$ specimens and (b) stoichiometric $TiNi_2Sn$ compound. As the fraction of Heusler content increases, the thermal conductivity decreases, reaching a minimum for $Ni_{1.15}$. For the two highest Ni samples, thermal conductivity is significantly higher and shows different behavior with temperature than the others. The calculated values of (c) κ_{el} and (d) κ_{lat} are presented as well.

Thermal Transport Properties

The thermal diffusivity of the materials was measured from room temperature to 875 K by the thermal flash method, using the Cowan model.[36] From this, the thermal conductivity was calculated using the relation $\kappa = \alpha * C_p * \rho$, where κ, α, C_p, and ρ are thermal conductivity, thermal diffusivity, specific heat capacity, and density, respectively. The Dulong-Petit law was used for C_p, which is known to underestimate the true heat capacity at elevated temperatures,[7] and densities were based on the geometry and mass of thermal diffusivity specimens.

The calculated thermal conductivity data is presented in Figure 12. The $x = 0.00$ material has the greatest thermal conductivity at room temperature, but also the largest slope with respect to temperature. In the high-temperature region, the thermal conductivity of TiNiSn is approximately equal to those of the $x = 0.05$ and 0.10 alloys. While $TiNi_{1.10}Sn$ is slightly less thermally conductive than $TiNi_{1.05}Sn$, the most pronounced decrease is in the $x = 0.15$ material. $TiNi_{1.15}Sn$ was less thermally conductive than TiNiSn by 30% at low temperatures, and remains the least conductive material through the whole measurement range. All biphasic materials exhibit a lower κ than the stoichiometric half-Heusler at low temperatures, despite the metallic nature of the $TiNi_2Sn$ phase. The measured thermal conductivity of $TiNi_2Sn$, plotted in Figure 12(b), is three to four times greater than the TiNiSn material for the entire temperature range. At higher temperatures, the reduction in κ is not as substantial: the lower four curves approach the same value, while the thermal conductivities of $TiNi_{1.20}Sn$ and $TiNi_{1.25}Sn$ exceed that of TiNiSn by as much 20-30%.

The total thermal conductivity in semiconductor materials is the sum of electronic, lattice and bipolar contributions. TiNiSn shows a bipolar component, as evidenced by an upturn in κ above a certain temperature while having a negative temperature dependence at lower T. The electronic contribution to the thermal conductivity was calculated using an SPB model[37,38] with $\kappa_{el} = \sigma LT$, where σ is the electrical conductivity, L is the Lorenz number, and T is the temperature. Lorenz numbers (not shown here) were determined from experimental Seebeck coefficients. The calculated L values of the studied materials are all 75% or less than that of the free electron model ($2.44\,W\Omega K^{-2}$), with the $x = 0.20$ and $x = 0.25$ samples exhibiting the highest Lorenz numbers, $\sim$1.8–1.9 $W\Omega K^{-2}$. The electronic thermal conductivity increases with increasing temperature which mirrors the increase in electronic conductivity. The samples with the highest full-Heusler fraction show the largest electronic thermal conductivities, as a larger amount of charge carriers are introduced by the metallic Heusler phase.

The primary contributor to the total thermal conductivity is the lattice thermal conductivity. Shown in Figure 12(d), the behavior gives insight into the phonon scattering behavior of the different samples. At room temperature, κ_{lat} first decreases for samples with $x =$ 0, 0.05, 0.1, 0.15 and then increases for samples with the highest full-Heusler fraction. This indicates that the phonon mean free path is disrupted by the secondary full-Heusler phase, since the thermal conductivity of the initial TiNiSn sample is the highest among all compounds. The lowest κ_{lat} was measured in $TiNi_{1.15}Sn$, which has about 9% of full-Heusler phase. At high temperatures, $TiNi_{1.20}Sn$ exhibts the largest value of κ_{lat}, likely due to the high degree of Heusler connectivity. The microstructure of $TiNi_{1.25}Sn$, while more Heusler-rich, is not seen to have such high connectivity, though a full 3-D analysis of structure is required to examine this in detail. This may explain why the material exhibits a similar slope to the $x = 0.20$ material, but more interfacial scattering, and thus lower κ_{lat}.

At high temperatures, κ_{el} increases such that it contributes more substantially to κ. This is reflected in the total thermal conductivity, wherein κ of the lower-Ni samples is dominated by the behavior of the half-Heusler bulk, yet a different temperature response is observed for $TiNi_{1.20}Sn$ and $TiNi_{1.25}Sn$.

Thermoelectric Figure of Merit

The thermoelectric figure of merit, ZT, is shown in Figure 13, as compiled from S, σ, and κ data. The measured peak ZT for stoichiometric TiNiSn is 0.35, which is comparable to values reported in literature for undoped TiNiSn. As x is raised from 0.00 to 0.15, the peak ZT in-

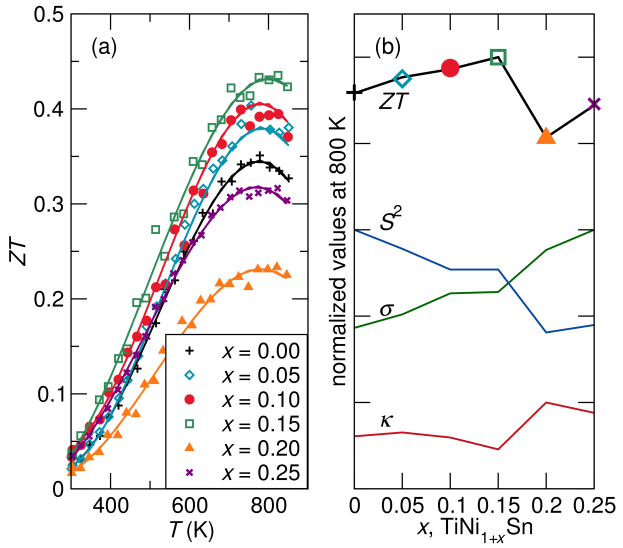

FIG. 13. (a)Thermoelectric figure of merit and (b) normalized values of the constituent properties (ZT, S^2, σ, and κ) at 800 K for each of the measured materials—S^2 is blue, σ is green, and κ is colored red. Peak ZT increases steadily with Ni content, x, before dropping for $Ni_{1.20}TiSn$ and $Ni_{1.25}TiSn$; this can largely be attributed to the changes in κ.

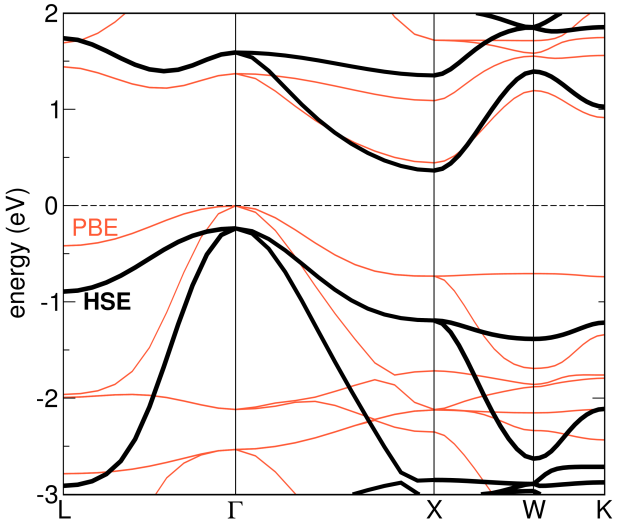

FIG. 14. Band structure of TiNiSn as calculated by DFT using the HSE06 hybrid functional. The compound is a semiconductor, with an indirect (Γ–X) band gap of 0.61 eV.

creases steadily, reaching a maximum of 0.44, measured on $TiNi_{1.15}Sn$. This 25% improvement is attributable to both the greater power factor and lower thermal conductivity.

In $TiN_{1.20}Sn$, the figure of merit drops precipitously, reaching a maximum ZT of 0.25. The ZT of the $x = 0.25$ material is higher, given its better power factor and lower κ than $x = 0.20$, but still fails to reach the values of the stoichiometric half-Heusler. Both alloys suffer from high thermal conductivities, and thus do not benefit from the biphasic constitution as the compounds of lower Ni content do.

Electronic Structure Calculations

To further explore the interplay between TiNiSn and $TiNi_2Sn$, first principles calculations were conducted for the two compounds. The central goals were to study the formation energies of the endmember compounds and to understand the nature of band energies at the interfaces in biphasic $TiNi_{1+x}Sn$. While we have previously reported the results of similar DFT study on band alignment in this system,[16] the calculations utilized GGA-PBE, whereas the present study was done using hybrid functionals. The authors are unaware of any published hybrid functional densities of states or band structure calculations or TiNiSn, which is also presented here.

Ionic and electronic relaxation of TiNiSn and $TiNi_2Sn$ primitive cells, containing three and four atoms, respectively, were run using LDA+U followed by HSE06. This was done to calculate the band structure with a method more accurate than PBE, which is known to underestimate the band gap in semiconductors.[39,40] The HSE06 half-Heusler TiNiSn band structure, which correctly predicts an indirect gap semiconductor, is shown in Figure 14, overlaid on the PBE band structure. While the hybrid functional band structure is qualitatively similar to previously reported calculations,[41,42] the Γ–X indirect band gap is found to be ∼33% wider, 0.61 eV as opposed to 0.45 eV. However, it should be noted that the existance of Ni interstials in the half-Heusler lattice—suggested by the increasing lattice parameters by XRD refinement—cause to "in-gap states," as observed in X-ray photemission spectroscopy (XPS) studies of TiNiSn.[14,43] These states lead to an experimental band gap of 0.12 eV,[44] much smaller than that calculated for the stoichiometric half-Heusler.

The densities of states (DOS) calculated for the stoichiometric compounds using hybrid functionals are displayed in Figure 15. Like the band structure, the half-Heusler DOS is similar to calculations presented in the literature. However, the $TiNi_2Sn$ DOS contains notable differences from the PBE calculation.[45] Though there is a moderate peak in the DOS around the Fermi level, E_F there are pseudogaps just below and above (∼ 100 meV). In both compounds, most states below E_F are filled Ni d-states while above sit unoccupied Ti d-states.

To examine the electronic interactions at the interface between the two phases, the band alignment was determined between TiNiSn and $TiNi_2Sn$. The local energy was calculated in supercells of "infinite" slabs in vacuum (overlayed on Fig. 16) and relaxed using GGA-PBE. By comparing the Fermi energies to these vacuum potentials, the band energies can be compared directly between TiNiSn and $TiNi_2Sn$. The results are shown in Figure 16. In the (110), close-packed orientation, the Fermi level of

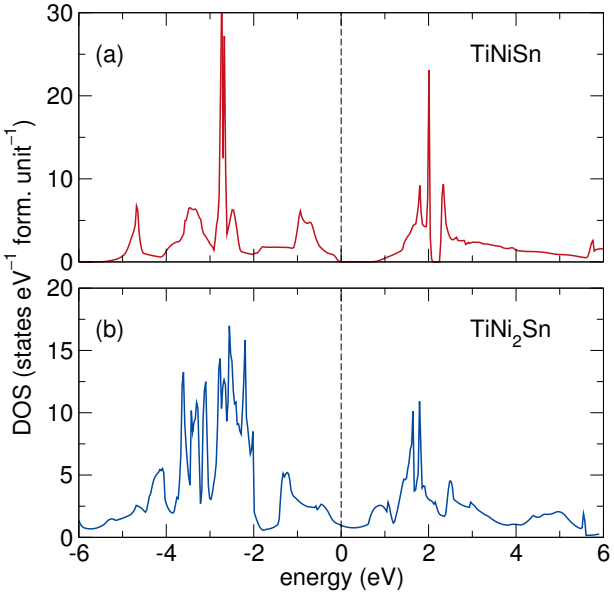

FIG. 15. Densities of states DFT calculations for (a) TiNiSn and (b) $TiNi_2Sn$ using HSE06 hybrid functional, referenced to the VBM and Fermi level, respectively. While qualitatively similar to PBE calculations, a pseudogap appears around the Fermi level of $TiNi_2Sn$.

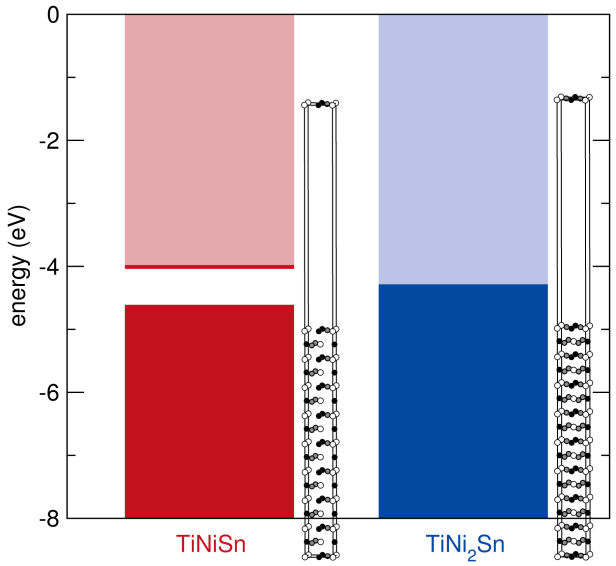

FIG. 16. Schematic representation of the positions of the VBM and CBM of TiNiSn and the E_F of $TiNi_2Sn$ with respect to vacuum, calculated with a (110) orientation. The Fermi level is in the center of the TiNiSn band gap, predicting a drawing of carriers at low temperatures. However, the VBM/E_F offset is small, 0.3 eV, suggesting ease of excitation at high temperatures. Supercells used for the calculation are included in the figure.

$TiNi_2Sn$ is in the center of the gap between the valence band maximum (VBM) and conduction band minimum (CBM) of TiNiSn.

Based on this band positioning, a depletion of charge cariers from the bulk should be expected upon Heusler addition into TiNiSn. Electrons excited from the VBM (TiNiSn is an n-type thermoelectric) would be drawn into the unoccupied states of $TiNi_2Sn$, lower in energy than the CBM. This result suggests that at 0 K, carriers are pulled from the semiconductor to the metal, as opposed to $TiNi_2Sn$ acting as a source of carriers. If the measured electrical conductivity curves from Figure 11(a) are extrapolated to 0 K, the biphasic samples would indeed have lower conductivities than the nominally stoichiometric material, however no low-temperature measurements were made in this study. The difference in energy levels is small, suggesting $TiNi_2Sn$ to be a favorable compound for alloying of TiNiSn thermoelectrics. The effect of Ni occupancy within the empty tetrahedral sites of TiNiSn was not calculated, due to prohibitively expensive computation time. Such a calculation may be elucidating.

CONCLUSIONS

We have studied the evolution of microstructure in a biphasic $TiNi_{1+x}Sn$, an alloying system suggested for increased efficiency of TiNiSn-based thermoelectrics. The solidification path, as explored through thermal analysis, makes it difficult to prepare phase-pure TiNiSn due to the formation of small amounts of other compounds during freezing depleting the liquid of solute. The half-Heusler phase lies in a lower temperature trough on the liquidus surface. The materials discussed here were prepared by induction melting and heat treatment, with no subsequent densification step. The off-stoichiometric materials were seen to phase segregate into TiNiSn and $TiNi_2Sn$, causing an increase in the measured ZT, due to a combination of increased power factor and decreased thermal conductivities. The presence of half-Heusler precipitates within the Heusler regions likely contributes further to the suppression of κ.

DFT calculations, show both that the E_f of $TiNi_2Sn$ sits between the TiNiSn VBM and CBM, while the E_g found by HSE06 is larger than given by PBE calculations. Also, the high stability of these compounds suggests that they are a good combination for biphasic Ti–Ni–Sn thermoelectric materials. However, with large Ni excess, the behavior of physical properties changes with respect to temperature, suggesting the existence of an optimal phase fraction and microstructure. The modest increase in ZT is encouraging as it was achieved without the introduction of heavier atoms on the Ti site (Hf, for instance, which is a relatively scarce element) or dopant atoms such as Sb. This suggests that there is room for further improvement in thermoelectrics through control of the composition, size and distribution of both phases.

ACKNOWLEDGEMENTS

This work was supported by the MRSEC Program of the National Science Foundation through DMR-1121053. J.E.D. is supported by the ConvEne IGERT Program (NSF-DGE 0801627). C.S.B. is a recipient of the Feodor Lynen Research Fellowship of the Alexander von Humboldt foundation. V.S.M. is supported by a U.C.S.B. Graduate Division Fellowship. We gratefully acknowledge many invaluable conversations with Prof. Alessandro Mottura and Dr. Jakoah Brgoch. We acknowledge support from the Center for Scientific Computing at the CNSI and MRL: an NSF MRSEC (DMR-1121053) and NSF CNS-0960316. Hewlett Packard is also acknowledged. This work made use of central facilities of the Materials Research Laboratory, supported by the MRSEC Program (DMR-1121053). Use of the Advanced Photon Source at Argonne National Laboratory was supported by the U. S. Department of Energy, Office of Science, Office of Basic Energy Sciences, under Contract No. DE-AC02-06CH11357. The Materials Research Laboratory is a member of the NSF-supported Materials Research Facilities Network

REFERENCES

[1] K. Smith and M. Thornton, Feasibility of Thermoelectrics for Waste Heat Recovery in Conventional Vehicles. NREL, U.S. Department of Energy, Ed., 2009.
[2] M. Zebarjadi, K. Esfarjani, Z. F. Ren, and G. Chen, Energy Environ. Sci. **5** (2012) 123702.[doi]
[3] J. R. Sootsman, D. Y. Chung, and M. G. Kanatzidis, Angew. Chem., Int. Ed. **48** (2009) 8616. [doi]
[4] S. Bhattacharya, T. M. Tritt, Y. Xia, V. Ponnambalam, S. J. Poon, and N. Thadhani. Appl. Phys. Lett. **81** (2002) 43.[doi]
[5] W. Kim, J. Zide, A. Gossard, D. Klenov, S. Stemmer, A. Shakouri, and A. Majumdar, Phys. Rev. Lett. **96** (2006) 045901.[doi]
[6] B. Yu, M. Zebarjadi, H. Wang, K. Lukas, H. Wang, D. Wang, C. Opeil, M. Dresselhaus, G. Chen, and Z. Ren, Nano Lett. **12** (2012) 2077.[doi]
[7] E. S. Toberer, A. Zevalkink, and G. J. Snyder, J. Mater. Chem. **21** (2011) 15843. [doi]
[8] K. Biswas, J. He, I. D. Blum, C.-I. Wu, T. P. Hogan, D. N. Seidman, V. P. Dravid, and M. G. Kanatzidis, Nature Lett. **489** (2012) 414 [doi]
[9] J. M. O. Zide, J.-H. Bahk. R. Singh, M. Zebarjadi, G. Zeng, H. Lu, J. P. Feser, D. Xu, S. L. Singer, Z. X. Bian, A. Majumdar, J.E. Bowers, A. Shakouri, and A. C. Gossard, J. Appl. Phys. **108** (2010) 123702.[doi]
[10] S.-W. Kim, Y. Kimura, Y. Mishima, Intermetallics **15** (2007) 349.[doi]
[11] H. Hohl, A. P. Ramirez, C. Goldmann, G. Ernst, B. Wölfing, and E. Bucher, J. Phys.: Condens. Matter **11,** 1697 (1999). [doi]
[12] T. Katayama, S.-W. Kim, Y. Kimura, and Y. Mishima, J. Electron. Mater. **32** (2003) 1160. [doi]
[13] Y. W. Chai and Y. Kimura, Appl. Phys. Lett. **100,** 033114 (2012).
[14] H. Hazama, M. Matsubara, R. Asahi, and T. Takeuchi. J. Appl. Phys. **110,** 063710 (2011).[doi]
[15] J. P. A. Makongo, D. K. Misra, X. Zhou, A. Pant, M. R. Shabetai, X. Su, C. Uher, K. L. Stokes, and P. F. P. Poudeu. J. Am. Chem. Soc. **133,** 18843 (2011).
[16] J. E. Douglas, C. S. Birkel, M.-S. Miao, C. J. Torbet, G. D. Stucky, T. M. Pollock, and R. Seshadri, Appl. Phys. Lett. **101** (2012) 183902.
[17] A. Zevalkink, E. S. Toberer, W. G. Zeier, E. Flage-Larsen, and G. J. Snyder, Energy Environ. Sci. **4** (2011) 510. [doi]
[18] C. Yu, T.-J. Zhu, R.-Z. Shi, Y. Zhang, X.-B. Zhao, and J. He, Acta Mater. **57,** 2757 (2009).
[19] Yu. V. Stadnyk and R. V. Skolozdra, Inorg. Mater. **27(10)** (1991) 1884.
[20] V. V. Romaka, P. Rogl, L. Romaka, Yu. Stadnyk, N. Melnychenko, A. Grytsiv, M. Falmbigl, and N. Skryabina, J. Solid State Chem. **197** (2013) 103. [doi]
[21] G. Baldinozzi, J.-F. Berar, M. Gautier-Soyer, and G. J. Calvarin, J. Phys. D.: Condens. Matter **9(45)** (1997) p. 9731. [doi]
[22] M. P. Echlin, A. Mottura, C. J. Torbet, and T. M. Pollock, Rev. Sci. Instrum. **83** (2012) 023701. [doi]
[23] G. Kresse and J. Furthmüller, Comp. Mater. Sci. **6** (1996) 15. [doi]
[24] G. Kresse, M. Marsman, and J. Furthmüller, Vienna Ab-Initio Simulation Package: VASP the GUIDE, (2012).
[25] G. Kresse and D. Joubert, Phys. Rev. B **59** (1999) 1758. [doi]
[26] J. P. Perdew, K. Burke, and M. Ernzerhof, Phys. Rev. Lett. **77** 3865 (1996).
[27] V. I. Anisimov, J. Zaanen, and O. K. Andersen, Phys. Rev. B **44** (1991) 943. [doi]
[28] J. Heyd, G. E. Scuseria, and M. Ernzerhof, J. Chem. Phys. **118** (2003) 8207.
[29] M. C. Flemings, *Solidification Processing*, (McGraw-Hill, New York, 1974).
[30] D.-Y. Jung, K. Kurosaki, C.-E. Kim, H. Muta, and S. Yama, J. Alloys Compd. **489** (2010) 328. [doi]
[31] H. Okamoto, J. Phase Equilib. Diff. **31** (2010) 202. [doi]
[32] H. Okamoto, J. Phase Equilib. Diff. **29** (2008) 297. [doi]
[33] K. Gupta, J. Phase Equilib. Diff. **20** (1999) 441. [doi]
[34] C. S. Birkel, W. Zeier, J. E. Douglas, B. Lettiere, C. Mills, G. Seward, A. Birkel, M. Snedaker, Y. Zhang, G. Snyder, T. M. Pollock, R. Seshadri, and G. Stucky, Chem. Mater. **24** (2012) 2558. [doi]
[35] J. Tobola, J. Pierre, S. Kaprzyk, R. Skolozdra, and M. Kouacou. J. Phys.: Condens. Matter **10** (1998) 1013. [doi]
[36] R. D. Cowan, J. Appl. Phys. **34** (1963) 926. [doi]
[37] A. F. May, E. S. Toberer, A. Saramat, and G. J. Snyder, Phys. Rev. B **80** (2009) 125205. [doi]
[38] A. F. May and G. J. Snyder, *Thermoelectrics Handbook: Thermoelectrics and its Energy Harvesting*, (2012).
[39] H. Xiao, J. Tahir-Kheli, and W. A. Goddard, J. Phys. Chem. Lett. **2** (2011) 212. [doi]
[40] J. A. Kurzman, M.-S. Miao, and R. Seshadri, J. Phys.: Condens. Matter **23** (2011) 465501.[doi]
[41] S. Öğüt and K. Rabe, Phys. Rev. B **51** (1995) 10443. [doi]
[42] M. Hichour, D. Rached, R. Khenata, M. Rabah, M. Merabet, and A. Reshak, J. Phys. Chem. Solids **73** (2012) 975. [doi]
[43] K. Miyamoto, A. Kimura, K. Sakamoto, M. Ye, Y. Cui, K. Shimada, H. Namatame, M. Taniguchi, S.-i. Fujimori, Y. Saitoh, E. Ikenaga, K. Kobayashi, J. Tadano, and T. Kanomata, Appl. Phys. Express **1** (2008) 081901. [doi]
[44] F. G. Aliev. Physica B **171** (1991) 199-205. [doi]
[45] J. Tobola, J. Pierre, S. Kaprzyk, R. Skolozdra, and M. A. Kouacou. J. Magn. Magn. Mater. **159** (1996) 192. [doi]
[46] T. Tokunaga, K. Hashima, H. Ohtani, and M. Hasebe. Mater. Trans., JIM **45** (2004) 1507. [doi]
[47] H. S. Liu, J. Wang, and Z. P. Jin. CALPHAD **28** (2004) 363. [doi]
[48] C. Colinet, J.-C. Tedenac, S. G. Fries. CALPHAD **33** (2009) 250. [doi]
[49] A. T. Dinsdale. CALPHAD **15** (1991) 317-425. [doi]